Developmental Cell, Volume *55*

Supplemental Information

Actin-Membrane Release Initiates Cell Protrusions

Erik S. Welf, Christopher E. Miles, Jaewon Huh, Etai Sapoznik, Joseph Chi, Meghan K. Driscoll, Tadamoto Isogai, Jungsik Noh, Andrew D. Weems, Theresa Pohlkamp, Kevin Dean, Reto Fiolka, Alex Mogilner, and Gaudenz Danuser

Method S1: Mathematical model and simulation, related to STAR methods

In this section of the supplement, we provide details on the basic ezrin-ratchet model, as well as variations referenced in the main text.

Spatial Model

The mathematical model of the ezrin ratchet system is based on the classical tethered ratchet model (Mogilner and Oster, 2003) and is graphically summarized in **Supplementary Figure 8**. The model describes the dynamics of three population densities along the leading edge of the cell: i) F-actin barbed ends, which we term working filaments, exert a force on the membrane through a polymerization ratchet (Mogilner and Oster, 1999), ii) ezrin-barbed end complexes, which we term linked filaments, serve as tether forces on the membrane, and iii) free ezrin, which binds to F-actin to form the complex. These three state variables, along with order-of-magnitude estimates of their values, are summarized in **Supplementary Table 1**. The estimated values are taken from previous modeling and experimental works (Grimm *et al.*, 2003; Schaus, Taylor and Borisy, 2007; Barnhart *et al.*, 2017). The spatial component of these densities corresponds to the thin strip along the leading edge of the cell described by the coordinate $0 < x < L$.

From **Supplementary Figure 8**, we note a key structural difference: in the classical tethered ratchet, new filaments enter the system as tethered. However, in this work, we assume this pool of tethered filaments is negligible compared to those that become transiently tethered after entering the system. Based on this, the dynamics of the model consist of first-order binding and unbinding reactions described in (1).

$$\begin{aligned}
\underbrace{\partial_t B}_{\text{free barbed ends}} &= \underbrace{D_B \partial_{xx} B}_{\text{diffusion}} + \underbrace{\alpha_0(1+\alpha_1 V)}_{\text{nucleation}} - \underbrace{\beta B}_{\text{capping}} - \omega E B + \gamma_0(1+\gamma_1 V)C \\
\underbrace{\partial_t C}_{\text{linked filaments complex}} &= D_C \partial_{xx} C + \underbrace{\omega E B}_{\text{association}} - \underbrace{\gamma_0(1+\gamma_1 V)C}_{\text{dissociation}} \\
\underbrace{\partial_t E}_{\text{local free ezrin}} &= D_E \partial_{xx} E + \underbrace{\kappa}_{\text{relaxation time}} (\underbrace{E_0}_{\text{average ezrin}} - E) + \underbrace{\sigma_E \Xi(x,t)}_{\text{spatiotemporal fluctuations}} \\
V &= V_0\left[1 - \left(\frac{\tau_0 + F_{\text{tether}} C}{B F_{\text{stall}}}\right)^{\lambda}\right].
\end{aligned} \tag{1}$$

- The return of free ezrin into the pool of E is neglected, as we are assuming there is not a limiting supply, but rather a pool that fluctuates slightly in space and time. The mean value of free ezrin is also normalized to $E_0 = 1$, as the effective binding rate ωE is the only quantity of interest, not the free ezrin level directly. The free ezrin pool and ezrin-associated filaments are known to be at lower concentrations (10-20x) than that of the free barbed ends (Tsai *et al.*, 2018).

- The velocity of the membrane depends on the force-per-barbed end and takes the functional form from empirical data (Keren *et al.*, 2008; Barnhart *et al.*, 2017).

- The branching rate increases with velocity (Carlsson, 2003; Barnhart *et al.*, 2017) due to complex geometric and mechanical effects. We consider a linear dependence on the velocity for simplicity.
- The disassociation rate between barbed ends and ezrin is also known to be force-dependent (Braunger *et al.*, 2014), and consequently velocity-dependent along the same line of reasoning as the classical tethered ratchet model
- The model neglects membrane retractions and instead has a minimum velocity of zero. However, the force-velocity curve could be modified easily to include negative velocities for appropriate forces without meaningfully changing the results of the model.

Unless noted otherwise, the parameters used in all simulations are described in **Supplementary Table 2**.

- The values of κ, σ_E are approximated from experimental measurements in this work (not shown). Specifically, the correlation time of ezrin fluctuations was seen to be $1/\kappa \approx 40[\mathrm{s}]$ and standard deviation approximately 10% of the baseline value, which is reproduced with these values. The diffusion in the spatial model dissipates fluctuations, so the value taken in this model is slightly higher than that taken in the nonspatial model, as noted in the table.
- The tether force F_{tether} reported in previous works (Mogilner and Oster, 2003) is an order of magnitude higher (tens of piconewtons), but we note that this force is proportional to the velocity of the membrane. Consequently, in this work, where the velocity is an order of magnitude slower, we expect tether forces on the magnitude of piconewtons.

The system of spatial PDEs (1) was simulated using a semi-implict Euler-Maruyama scheme (Lord, Powell and Shardlow, 2014) with timestep `dt = 10e-3` until `tmax = 800` with 301 spatial grid points. A typical trajectory of the spatial model can be seen in **Supplementary Figure 9**.

From **Supplementary Figure 9**, we see that the mathematical model demonstrates transient protrusive behavior akin to the metastable switching of the canonical stochastic Allen-Cahn equation(Berglund, 2019). From these simulations, we also note that protrusive activity correlates with low free ezrin levels. To understand this relationship more quantitatively, we turn to a simpler (nonspatial) model.

Nonspatial model

Spatial variations occur at a spatial scale that coincides with the windows of the experimental setup (microns) due to the relatively small diffusivities of the quantities in the system. Consequently, for ease of analysis, we instead study a non-spatial system with the same state variables as the spatial model, with the interpretation that these quantities are constant in each experimental spatial window. The nonspatial model is then

$$\begin{aligned}
\frac{\mathrm{d}B}{\mathrm{d}t} &= \alpha_0(1+\alpha_1 V) - \beta B - \omega E B + \gamma_0(1+\gamma_1 V)C \\
\frac{\mathrm{d}C}{\mathrm{d}t} &= \omega E B - \gamma_0(1+\gamma_1 V)C \\
\frac{\mathrm{d}E}{\mathrm{d}t} &= \kappa(E_0 - E) + \sigma_E \qquad \underbrace{\xi(t)}_{\text{temporal fluctuation}} \qquad\qquad (2) \\
V &= V_0\left[1 - \left(\frac{\tau_0 + F_{\text{tether}}C}{BF_{\text{stall}}}\right)^{\lambda}\right].
\end{aligned}$$

Statistics of protrusions in the experimental setup are computed on a window-by-window basis, and therefore are inherently nonspatial. Therefore, the main text figures, all statistics of the model (e.g. protrusion durations) are describing those obtained from the nonspatial system (2).

Stability & equilibria analysis

Although determining the equilibria (and stability thereof) of (2) is feasible, it becomes considerably less wieldy in the limit that $\lambda \to \infty$, so the force-velocity curve becomes a sharp threshold. For the remainder of this subsection, we make that assumption.

In this limit, the force-velocity curve becomes

$$V = V_0 \mathbf{1}_{\frac{\tau_0 + F_{\text{tether}}C}{BF_{\text{stall}}} < 1}.$$

where $\mathbf{1}_{(\cdot)}$ is 1 whenever the condition $(\cdot)$ is true and zero otherwise. Consequently, the behavior of the model can be split into two regimes:

Regime 1: $\tau_0 + F_{\text{tether}}C > BF_{\text{stall}}$, $V = 0$.

Regime 2: $\tau_0 + F_{\text{tether}}C < BF_{\text{stall}}$, $V = V_0$.

We now derive the conditions such that each of these regimes provides a basin of attraction for a stable steady state, separated by the separatrix $\tau_0 + F_{\text{tether}}C = BF_{\text{stall}}$. In both regimes, $E(t) \to E_0$ stably.

Regime 1. Taking $E(t) = E_0$ and $V = 0$, The system (2) becomes

$$\begin{aligned}
\frac{\mathrm{d}B}{\mathrm{d}t} &= \alpha_0 - \beta B - \omega E_0 B + \gamma_0 C \\
\frac{\mathrm{d}C}{\mathrm{d}t} &= \omega E_0 B - \gamma_0 C.
\end{aligned} \qquad (3)$$

The system (3) has an equilibrium

$$B_1^\star = \frac{\alpha_0}{\beta}, \qquad C_1^\star = \frac{E_0 \omega \alpha_0}{\beta \gamma_0}.$$

Regime 2. Taking $E(t) = E_0$ and $V = V_0$ normalized to 1, The system (2) then becomes

$$\begin{aligned}
\frac{\mathrm{d}B}{\mathrm{d}t} &= \alpha_0(1+\alpha_1) - \beta B - \omega E_0 B + \gamma_0(1+\gamma_1)C \\
\frac{\mathrm{d}C}{\mathrm{d}t} &= \omega E_0 B - \gamma_0(1+\gamma_1)C.
\end{aligned} \qquad (4)$$

The system (4) has an equilibrium

$$B_2^\star = \frac{\alpha_0(1+\alpha_1)}{\beta}, \qquad C_2^\star = \frac{E_0\omega\alpha_0(1+\alpha_1)}{\beta\gamma_0(1+\gamma_1)}.$$

Thus, the conditions for these to both be stable correspond to them appearing in each of the appropriate regimes, so for region 1, substituting the equilibrium to the inequality condition yields

$$\tau_0 + F_{\text{tether}} C_1^\star > B_1^\star F_{\text{stall}},$$

which provides the condition

$$F_{\text{stall}} \frac{\alpha_0}{\beta_0} < \tau_0 + \frac{F_{\text{tether}} E_0 \omega}{\gamma_0}. \text{ (5)}$$

Condition (5) effectively says that a stall state exists if the steady-state force per working filament is smaller than the combination of membrane tension and tethered filaments. Similarly, in regime 2, we have

$$\tau_0 + F_{\text{tether}} C_2^\star < B_2^\star F_{\text{stall}}$$

yielding

$$F_{\text{stall}} \frac{\alpha_0(1+\alpha_1)}{\beta_0} < \tau_0 + \frac{F_{\text{tether}} E_0 \omega}{\gamma_0(1+\gamma_1)}, \text{ (6)}$$

which has the same interpretation: during a protrusive event, the force per filament must be lowered due to the increased detachment rate of ezrin from filaments. Combining the conditions (5) and (6) yields the simultaneous condition

$$\frac{\gamma_0(\alpha_0 F_{\text{stall}} - \beta\tau_0)}{\omega\alpha_0 F_{\text{tether}}} < E_0 < \frac{\gamma_0(\gamma_1+1)(\alpha_0(\alpha_1+1)F_{\text{stall}} - \beta\tau_0)}{\omega\alpha_0(\alpha_1+1)F_{\text{tether}}}. \text{ (7)}$$

Although the functional form of (7) is complex, the lesson is intuitive: to drive transient protrusive events with this model, the baseline ezrin level must be at an intermediate sweet-spot where too little ezrin would have constant velocity but too much would have no protrusive activity at all.

With this analysis, we now understand protrusive events in the nonspatial model as metastable switching between the two equilibria across the separatrix (barrier), as seen in **Supplementary Figure 10a**. We note that the simulations use a finite λ and therefore have true equilibria that deviate slightly from the ones used for the analysis. Consequently, the simulation seen in the figure does not relax to exactly the predicted equilibria, but still demonstrates the qualitative behavior.

Furthermore, this analysis gives us insight toward the interplay of actin and ezrin levels, as seen in **Supplementary Figure 10b**. So long as the branching rate is sufficiently high to overcome membrane tension, ezrin levels primarily dictate the protrusive behavior. That is, moving vertically in the diagram (changing actin levels) produces little difference in regime in contrast to moving horizontally (changing ezrin levels).

Model experiments

In this section, we describe in more detail the experiments run on the mathematical model presented in the main text.

Actin vs. ezrin fluctuations

To explore how different sources of stochasticity influence protrusions, we slightly modify the model by removing ezrin fluctuations and adding actin fluctuations. This is of natural interest out of the possibility that just fluctuations in the number of barbed ends (or Arp2/3 levels) could drive protrusions. Specifically, in these simulations, we take $\sigma_E = 0$ and change the dynamics of the barbed ends, $B(t)$ to be

$$\frac{\mathrm{d}B}{\mathrm{d}t} = \alpha_0(1+\alpha_1 V) - \beta B - \omega E B + \gamma_0(1+\gamma_1 V)C + \sigma_B \xi(t)$$

with $\sigma_B = 25$. The result of these simulations, compared with the original model can be seen in main text figures 2C and 2D. From these, we find a critical conclusion: fluctuations in actin seemingly *cannot* drive protrusion events. The reason for this is as follows: If the ezrin pool is sufficient, then if the amount of barbed ends fluctuates larger than its baseline value, some fraction of these barbed ends will become tethered to ezrin, meaning the ratio of free to tethered barbed ends remains relatively unchanged, disallowing a protrusive event. However, if the free ezrin fluctuates, this ratio of free to tethered barbed ends may change significantly, allowing for protrusions. This is summarized graphically in **Supplementary Figure 11**.

Introduction of high-affinity ezrin

The introduction of ezrin TD was simulated in the model by introducing a separate pool of ezrin with higher affinity (Tsai *et al.*, 2018), but structurally looks no different. Call this second population $\tilde{E}(t)$. Then, the system (2) becomes

$$\begin{aligned}
\frac{\mathrm{d}B}{\mathrm{d}t} &= \alpha_0(1+\alpha_1 V) - \beta B - \omega E B - \tilde{\omega}\tilde{E}B + \gamma_0(1+\gamma_1 V)(C+\tilde{C}) \\
\frac{\mathrm{d}C}{\mathrm{d}t} &= \omega E B - \gamma_0(1+\gamma_1 V)C \\
\frac{\mathrm{d}\tilde{C}}{\mathrm{d}t} &= \tilde{\omega}\tilde{E}B - \gamma_0(1+\gamma_1 V)\tilde{C} \\
\frac{\mathrm{d}E}{\mathrm{d}t} &= \kappa(E_0 - E) + \sigma_E E_0 \xi(t) \\
\frac{\mathrm{d}\tilde{E}}{\mathrm{d}t} &= \kappa(\tilde{E}_0 - \tilde{E}) + \sigma_{\tilde{E}} \tilde{E}_0 \tilde{\xi}(t)
\end{aligned}$$

To explore how the relative quantities of regular and TD ezrin contribute, we take $E_0 + \tilde{E}_0 = 1$. Experimental measurements indicate roughly equal pools of WT and TD ezrin (Supplementary Figure 3), so both E_0 and $\tilde{E}_0$ are set to 0.5. TD ezrin differs from the WT variety in the model by having a higher affinity $\tilde{\omega} > \omega$ and slightly larger fluctuations, the latter of which was experimentally observed as shown in Modeling Supplement Figure 5. Specifically, we set $\tilde{\omega} =$

$10\ \omega$ based on the calculation in this supplement and $\sigma_{\tilde{E}} = 1.75\sigma_E$ from observations that TD ezrin pool had fluctuations 1.5-2x the size of the WT ezrin pool. Adding higher affinity ezrin intuitively decreases the protrusion activity in the model.

Varying Arp2/3 expression

Arp2/3 levels are not directly included in the model, but the F-actin nucleation/branching term is assumed to be Arp2/3-mediated, and therefore manifests in the model in that way. Thus, to simulate varying the Arp2/3 levels at the leading edge, α_0, the branching rate varied from 50% of its original value (underexpressed) to 150% of its original value (overexpressed). Qualitatively, as Arp2/3 levels and therefore branching increases, there is an increase in protrusive activity.

This seems like it contradicts the point that actin fluctuations cannot drive protrusions, but it is a distinct point. Increasing α_0 increases the total amount of F-actin in the system, which does not initiate a protrusive event on its own. The velocity is determined by not only the ratio of the working and tethered filaments, but also the inherent membrane tension. Consequently, increasing the overall levels of actin does not affect the ratio of filaments but does help overcome the membrane tension, driving the system closer to a protrusion event overall.

Model sensitivity analysis

Sensitivity analysis was performed by normalizing the relative effect of a parameter change, measured in each of protrusion frequency, duration, and velocity, by the relative change in that parameter. The statistical comparison shown in Figure 6 is a t-test of the means of the model sensitivities calculated for the following parameter values that modulate arp2/3 activity and ezrin affinity. Simulated protrusion duration showed no significant difference due to changes in either arp2/3 activity or ezrin affinity (data not shown).

Supplementary Figures

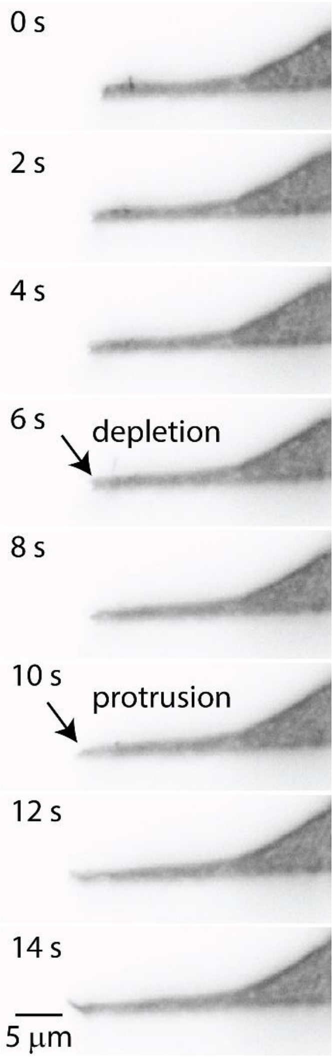

Supplementary Figure 1. Side view of GFP-ezrin during protrusion (Related to Figure 2). Lateral-axial (i.e., x-z) reslice of light sheet fluorescence image of GFP-ezrin in U2OS cells showing that within the diffraction limit, nascent protrusions do not appear thinner than other lamellipodial regions.

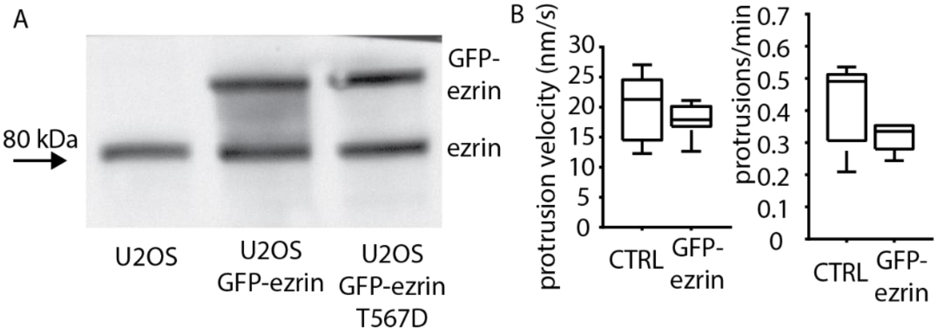

Supplementary Figure 2. Relative expression of wild type and mutant ezrin in U2OS cells (Related to Figure 3). (A) Western blot for ezrin showing the relative abundance of endogenous (unlabeled) ezrin compared to the exogenous (GFP-tagged) ezrin in cells expressing wild type and mutant ezrin. (B) Protrusion velocity and frequency in cells expressing GFP-ezrin compared to control cells. Neither comparison is statistically significant. Plots show the distribution of the means within a cell; p=0.48 t test for velocity, p=0.70 Mann-Whitney test for velocity, p=0.1389 t test for frequency, p=0.19 Mann-Whitney test for frequency, n=12 cells for GFP-ezrin and n=9 control cells.

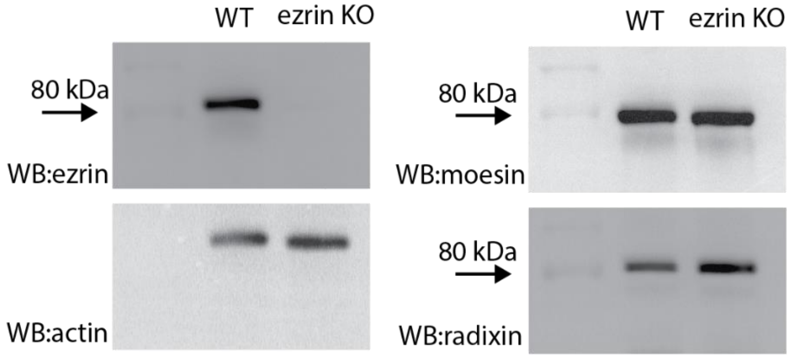

Supplementary Figure 3. Change in ERM family emember expression upon ezrin knock out (Related to Figure 4). Western blots showing expression level of ezrin, radixin and moesin in parental and ezrin knockout cells.

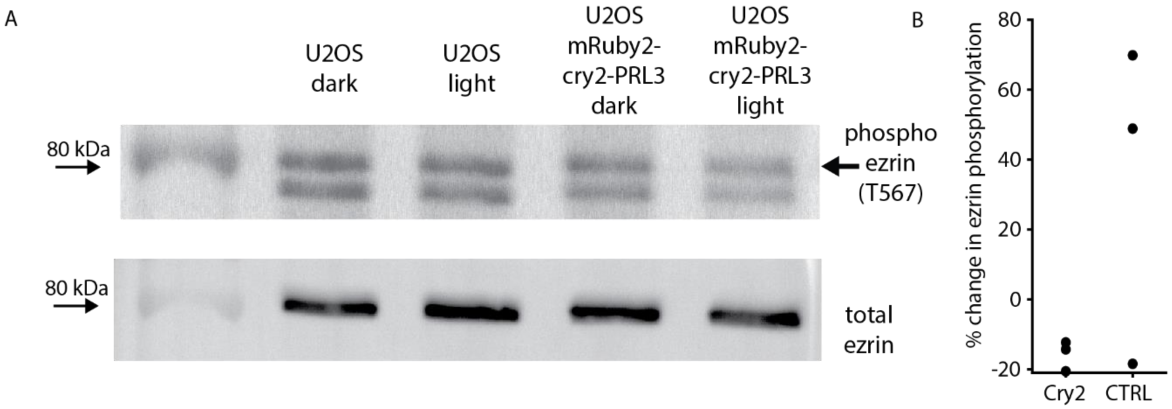

Supplementary Figure 4. Dephosphorylation of ezrin via light-activated PRL3 (Related to Figure 4). (A) Western blot showing change in ezrin phosphorylation due to whole-cell photorecruitment of mRuby2-cry2-PRL3 construct compared to control cells. (B) Quantification of Western blots from three separate experiments showing the effect of light on ezrin phosphorylation in cells expressing mRuby2-cry2-RPL3 and CIBN-CAAX when exposed to light, compared to control cells.

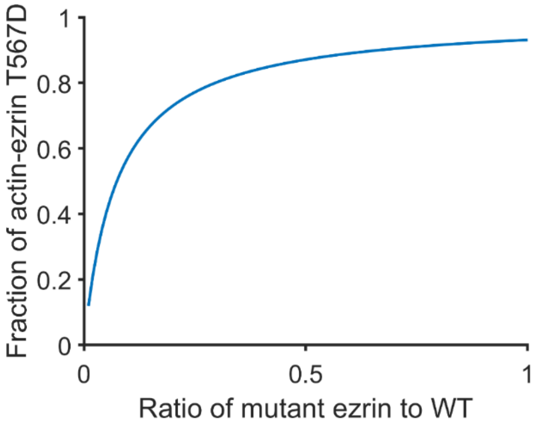

Supplementary Figure 5. Relative fraction of mutant and wild type ezrin bound to actin (Related to Figure 5). Model simulation results showing theoretical fraction of ezrin bound to actin that is the mutant form as a function of different simulated expression ratios of WT and mutant ezrin.

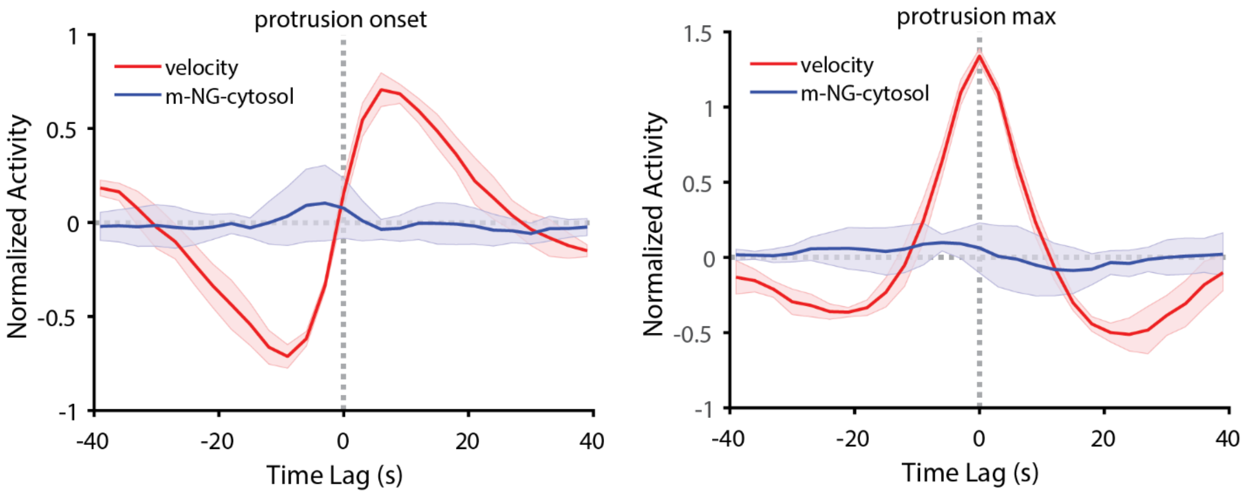

Supplementary Figure 6. Control experiment to determine if relationship between GFP-ezrin and edge protrusion is due to changes in cytosolic volume (Related to STAR Methods). Normalized edge velocity and cytosolic fluorescence intensity, aligned to protrusion onset (left) and protrusion maximum (right) in U2OS cells.

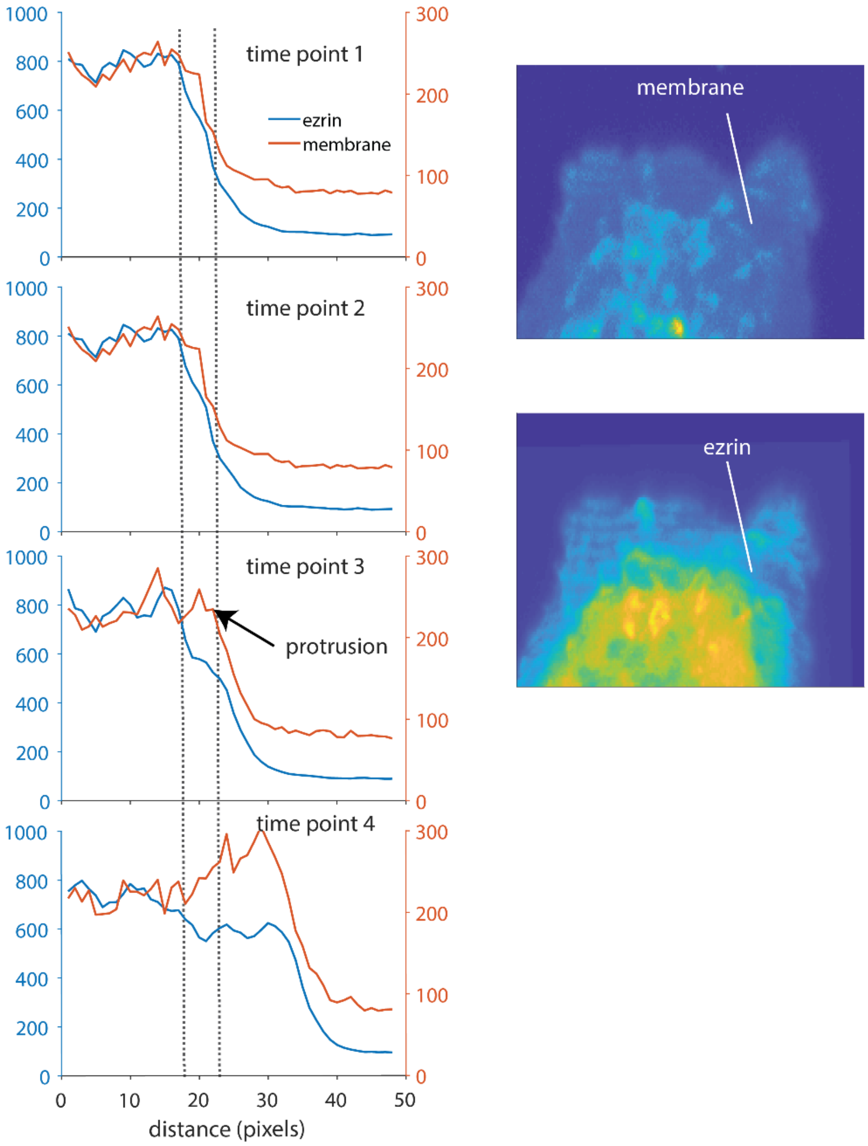

Supplementary Figure 7. Ezrin depletion during protrusion (Related to STAR Methods). Linescan analysis of GFP-ezrin and membrane marker intensity in a U2OS cell imaged using light sheet microscopy, showing that membrane protrusion precedes a recovery in GFP-ezrin following protrusion.

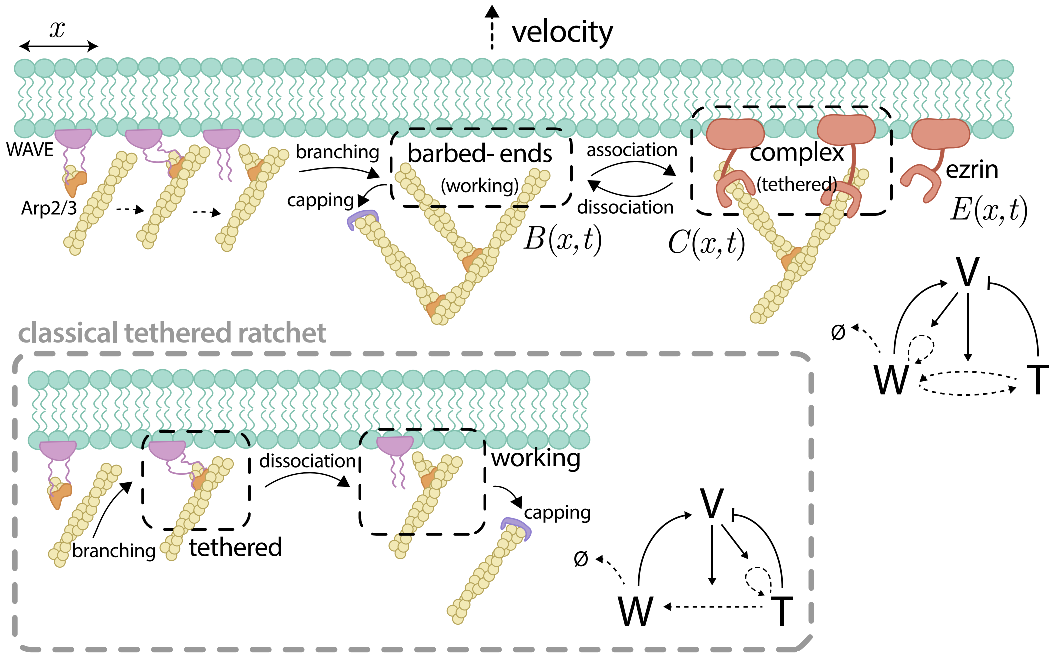

Supplementary Figure 8. Comparison of actin ratchet models **(**related to STAR Methods). Cartoon schematic of the proposed actin release model (top), contrasted with the classical tethered ratchet model (Mogilner and Oster, 2003).

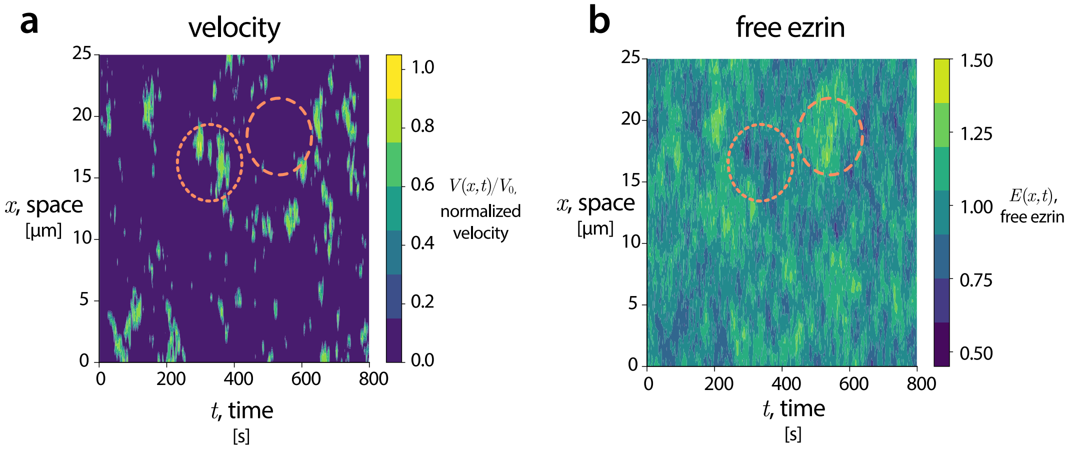

Supplementary Figure 9. Spatial simulation of the actin release model (related to STAR Method). Typical simulation of the spatial system, (1). On the left, the instantaneous velocity is determined by the relative quantities of free and tethered filaments. On the right, the density of free ezrin. The two highlighted regions qualitatively demonstrate that high protrusive activity corresponds to low ezrin free levels (dotted) and low protrusive activity corresponds to high ezrin levels (dashed).

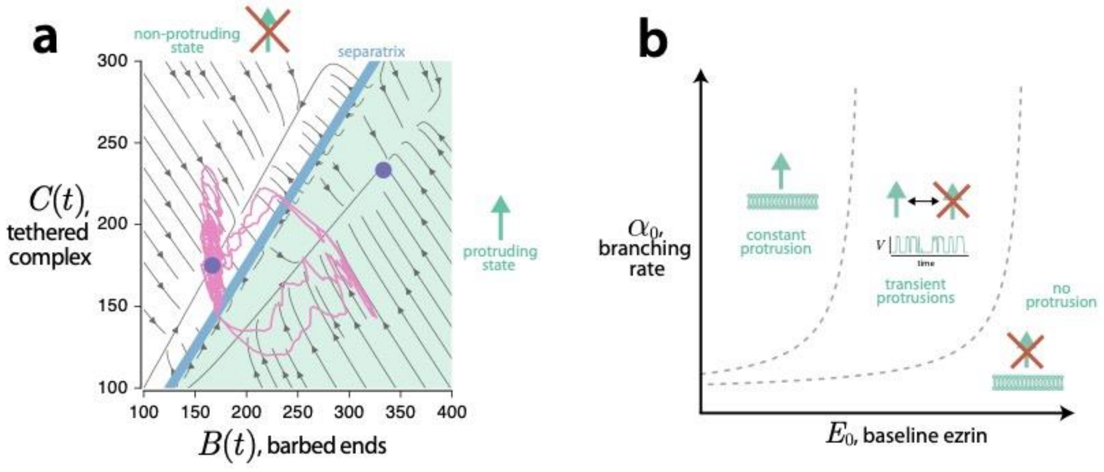

Supplementary Figure 10. Phase analysis of the actin release model (related to STAR Methods). On the left: a phase portrait of the typical simulation (with ezrin fluctuations) seen in the main text as a function of the number of barbed ends and linked filament complexes. Protrusive events can be interpreted as a metastable switch across the separatrix. The two stable equilibria are labeled in purple circles. On the right: the condition (7) as a function of the baseline ezrin level E_0 and branching rate α_0.

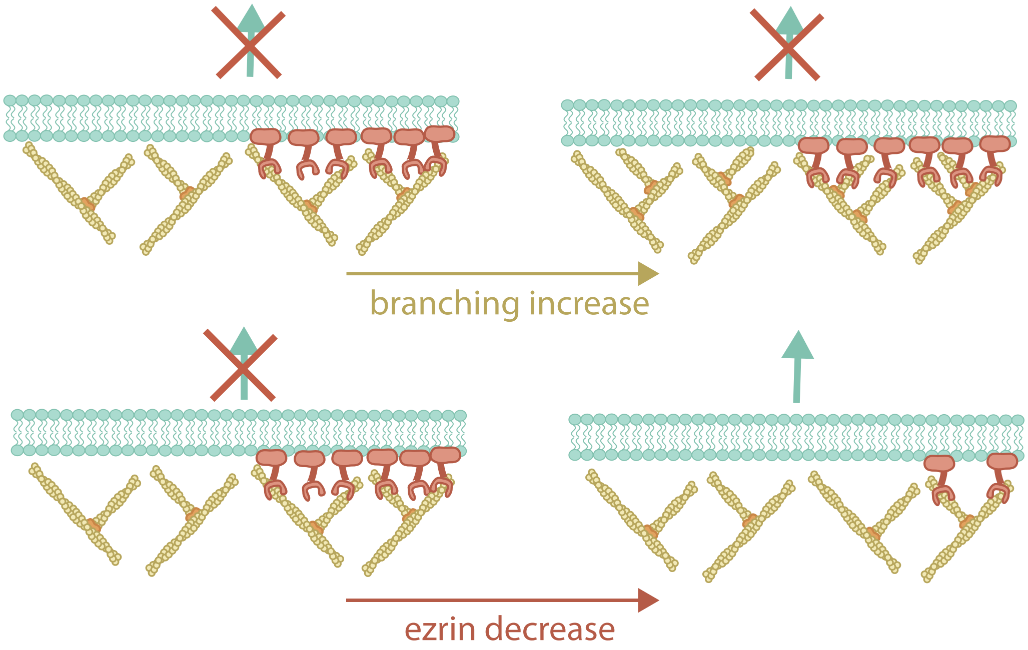

Supplementary Figure 11. Graphical conceptualization of the actin release model (related to STAR Method). Cartoon explaining the fundamental difference between actin (or Arp2/3) fluctuations and ezrin fluctuations. Actin fluctuations do not alter the ratio of working to tethered, and therefore cannot drive protrusions. However, ezrin fluctuations do alter this ratio and can initiate protrusions.

Supplementary Table 1. State variables of the spatial system (related to STAR Method).

state variable	**meaning**	**range**
$B(x,t)$	density of F-actin working filaments (free barbed ends)	hundreds per μm
$C(x,t)$	density of linked filaments (tethered barbed ends)	hundreds per μm
$E(x,t)$	*normalized* density of free ezrin	1 per μm

Supplementary Table 2. Parameter values used for the mathematical model *(*related to STAR Methods). The dagger symbol (†) denotes parameters used only in the nonspatial version of the model.

parameter	Meaning	range/source	value used
D_B	barbed end diffusivity	$\sim v^2\beta$ tenths of μm^2/s (Grimm *et al.*, 2003)	$.025$ [μm^2/s]
α_0	barbed end branching rate	tens to hundreds per μm per second (Grimm *et al.*, 2003)	$50[1/(\mu\text{m} \cdot \text{s})]$
α_1	branching rate increase from velocity	0.5 to 2, estimated from data in (Keren *et al.*, 2008; Mueller *et al.*, 2017)	1
β	capping rate	tenths per second (Grimm *et al.*, 2003)	$.3[1/\text{s}]$
ω	barbed-end ezrin association rate	seconds (Fritzsche, Thorogate and Charras, 2014)	2.1 $[1/\text{s}]$
γ_0	barbed-end ezrin dissociation rate	seconds (Fritzsche, Thorogate and Charras, 2014)	2 $[1/\text{s}]$
γ_1	barbed-end ezrin dissociation rate increase	0.5 to 2, estimated from data in (Braunger *et al.*, 2014)	0.5
D_C	barbed-end/ezrin complex diffusivity	slow (Fritzsche, Thorogate and Charras, 2014)	10^{-4} [μm^2/s]
D_E	free ezrin diffusivity	hundreths (Fritzsche, Thorogate and Charras, 2014) to tenths (Coscoy *et al.*, 2002) of μm^2	0.1 [μm^2/s]
κ	relaxation time of ezrin fluctuations	estimated from data $\sim$ tenths of seconds	0.025 $[1/\text{s}]$
σ_E	magnitude of WT ezrin fluctuations	estimated from data $\sim$ 10%	$.045, .03^\dagger$
E_0	mean level of ezrin	normalized	1 $[1/\mu\text{m}]$
τ_0	cortical tension	tens to hundreds of pN per μm (Grimm *et al.*, 2003; Mogilner and Oster, 2003; Keren *et al.*, 2008; Barnhart *et al.*, 2017)	25 [pN/μm]
F_0	stall force per filament	piconewtons/filament (Grimm *et al.*, 2003; Mogilner and Oster, 2003)	1 [pN]
λ	steepness of force-velocity curve	$\sim 4 - 8$ (Zhu and Mogilner, 2012)	4
F_{tether}	tether force	piconewtons, estimated (Mogilner and Oster, 2003)	1 $[pN]$
L	domain size	experimental observations	25 $[\mu\text{m}]$